Generation of a Nondiffracting Superchiral Optical Needle for Circular Dichroism Imaging of Sparse Subdiffraction Objects

Haifeng Hu,[1,2] Qiaoqiang Gan,[1,3,*] and Qiwen Zhan[1,4,†]
[1]School of Optical-Electrical and Computer Engineering, University of Shanghai for Science and Technology, Shanghai, 200093, China
[2]College of Information Science and Engineering, Northeastern University, Shenyang, 110819, China
[3]Department of Electrical Engineering, The State University of New York at Buffalo, Buffalo, New York 14260, USA
[4]Department of Electro-Optics and Photonics, University of Dayton, 300 College Park, Dayton, Ohio 45469-2951, USA

(Received 2 January 2019; published 7 June 2019)

Chirality describes not only the structural property of three-dimensional objects, but also an intrinsic feature of electromagnetic fields. Here we report a strategy to realize a Bessel beam superchiral "needle" by focusing a twisted radially polarized beam on a planar dielectric interface. By tailoring the light spatial distribution in the pupil plane of a high numerical aperture lens, the chirality of the local field at the focus can be enhanced by 11.9-fold than that of a circular polarized beam. Through a combined interaction of chiral and achiral transitions, the dimension of the region with enhanced chiral sensitivity can be shrunk down to $\lambda/25$. This theoretical work paves the way towards a completely new label-free imaging technique using the enhanced circular dichroism for sparse subdiffraction chiral objects (e.g., individual molecules).

DOI: 10.1103/PhysRevLett.122.223901

Chirality describes the structural property of a three-dimensional object, whose mirror image cannot be superimposed on its original image. This is a common feature for many biochemical molecules, such as amino acids and sugars. In biochemical and pharmaceutical industries, it is important to distinguish and separate the molecules with opposite chiralities (i.e., enantiomers) due to their different toxicities. For a chiral molecule, the absorption rates (i.e., A^+ and A^-) under the excitation of left- and right-handed circularly polarized light (CPL) are different. To distinguish opposite enantiomers, the dissymmetry factor (i.e., g factor) is defined as $g = 2(A^+ - A^-)/(A^+ + A^-)$, which is measured in conventional circular dichroism (CD) spectroscopy [1]. Because of the large mismatch between the molecule size and the wavelength of the electromagnetic (EM) wave, CD signals are usually weak and difficult to measure (a typical value of g is 10^{-3} to 10^{-6}) [2]. In addition, conventional CD spectroscopy was used to measure samples over a large area. One cannot distinguish chirality information of individual molecules but measure the average property of a large number of chiral molecules only. To realize imaging-based CD spectroscopy with spatial optical resolution, the chiral optical response of individual molecule is required to be enhanced, which is the focus of this work.

For an isotropic molecule whose chirality originates from the coupling between electric dipole (ED) and magnetic dipole (MD), its response to the monochromatic EM field can be described by [1]

$$\mathbf{p} = \mu_E \mathbf{E} - iG\mathbf{B}, \quad \mathbf{m} = \mu_B \mathbf{B} + iG\mathbf{E}, \tag{1}$$

where $\mathbf{p}$ and $\mathbf{m}$ are the ED moment and MD moment related to the local EM fields $\mathbf{E}$ and $\mathbf{B}$, respectively. μ_E, μ_B, and G are the electric, magnetic, and mixed electric-magnetic dipole polarizabilities. The CD measurements can be generalized for an arbitrary excitation field whose chirality is switched by applying the parity inversion (i.e., $\mathbf{E} \to -\mathbf{E}$, $\mathbf{H} \to \mathbf{H}$). It has been proved that the g factor in this generalized case is not only determined by chiral properties of molecules, but also by the chirality of the EM field [3]. A term of "superchirality" was introduced to reveal larger g factors of chiral molecules than those obtained under the illumination of CPL (i.e., $g/g_{\mathrm{CPL}} > 1$). The superchirality condition for a monochromatic EM field can be expressed by [4]

$$g/g_{\mathrm{CPL}} = \frac{\mathrm{Im}(\mathbf{E} \cdot \mathbf{H}^*)}{(1/Z_0)|\mathbf{E}|^2} > 1. \tag{2}$$

Here Z_0 is the wave impedance in the vacuum. The numerator of Eq. (2) should fulfill the relationship of $\mathrm{Im}(\mathbf{E} \cdot \mathbf{H}^*) \le |\mathbf{E}||\mathbf{H}|$. In this case, $g/g_{\mathrm{CPL}} \le Z_0|\mathbf{H}|/|\mathbf{E}|$. Consequently, the necessary condition for the superchiral EM field is $|\mathbf{H}|/|\mathbf{E}| > 1/Z_0$.

For the homogeneously polarized beam, $|\mathbf{H}|/|\mathbf{E}| = 1/Z_0$ is a constant. But for some particular inhomogeneous EM fields, it is possible to obtain superchirality in local regions [3–8]. For example, superchiral light can be generated at the nodes of a standing wave induced by two coherent CPL beams with opposite chirality and propagation directions [3,5]. Unfortunately, in this configuration, the thickness of the superchiral region ($g/g_{\mathrm{CPL}} > 1$) is only

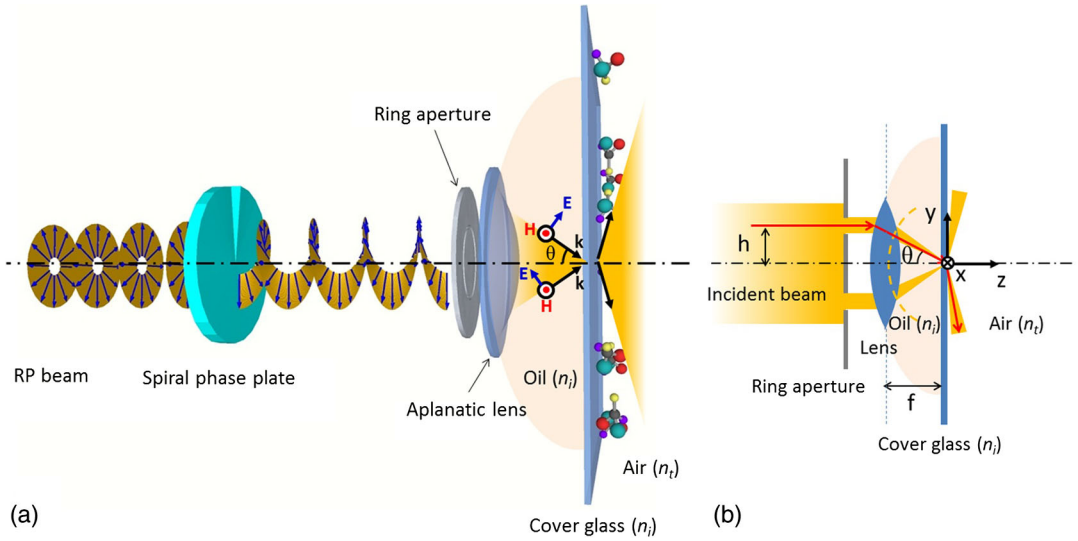

FIG. 1. (a) Schematic of the system to generate a superchiral field by focusing a twisted RP beam. (b) Theoretical model to calculate the EM field distribution near the focus. f is the focus length of the lens, and h is the lateral position of the incident ray.

0.032λ and it is not resolved in the orthogonal direction. Technically, it is difficult to immobilize chiral molecules within this region [3]. Recently, an alternative strategy was reported to create lattices of the superchiral field using spatial engineering of complicated optical fields (e.g., the superposition of multi plane waves [4,6,9]). Building upon this pioneering concept, in this work, we theoretically address the major barrier for imaging based CD spectroscopy: i.e., a strategy to generate a single deep subwavelength superchiral hot spot using an engineered high-numerical-aperture (NA) focusing system. Importantly, this deep subwavelength spot extends into the z direction by more than 10 wavelengths, resulting in a unique optical Bessel "needle." Therefore, the heavy dependence on the local region proposed by the previous superchiral strategy [3] is largely avoided. This method will enable the ability to scan the optical response of the chiral sample dynamically by moving the subwavelength needle, and therefore enable the observation of the chirality of sparse subdiffraction objects with the spatial localization capability determined by the size of the superchiral spot.

Here we first explain the general design principle of the proposed strategy. The optical system to generate the superchiral hot spot is illustrated in Fig. 1(a). A radially polarized (RP) beam passing through a spiral phase plate (SPP) and a ring aperture is tightly focused on the planar dielectric interface of the cover glass (more technical details of components used in our modeling are provided in Sec. I of the Supplemental Material [10]). In this case, the chirality of the beam is modified by the topological handedness of its wave front. In recent years, this type of tightly focused cylindrical vector beam has attracted extensive attention [16–19]. Importantly, the magnetic and electric fields of the focused vector beam are well spatially separated [20–23] (it should be noted that those previously reported spatially separated EM fields produced at the focus do not increase the optical chirality). Therefore, the ratio of $|\mathbf{H}|/|\mathbf{E}|$ can be much larger than $1/Z_0$ in a confined volume, which is a necessary condition to realize superchiral EM fields.

To validate this design principle, we then employ the Richards-Wolf method [24,25] (see Sec. II in the Supplemental Material [10]) to calculate the EM field distribution near the focus. At the focal point, the EM field can be expressed by the angular spectrum representation, which is actually the superposition of plane waves towards different propagation directions. Each plane wave in the angular spectrum representation of the focused field originates from a specific ray refracted by the lens as illustrated in Fig. 1(b). The lateral position of the incident ray and the incident angle θ of the refracted ray has the relationship of $h = f\sin\theta$, where f is the focal length of the lens. The range of the incident angle $[\theta_{\min}, \theta_{\max}]$ can be controlled by the ring aperture. We then explore the relationship between the incident angle and g/g_{CPL}.

To simplify the analysis, the focused field under an individual incident angle θ is considered. The topological charge of the SPP is $m = 1$ in this modeling. The θ-dependent g/g_{CPL} on the dielectric plane (as well as the focal plane) can then be expressed as

$$\frac{g(\rho,\theta)}{g_{\mathrm{CPL}}} = \frac{2\mathrm{Re}[\Theta(\theta)]\mathrm{Im}[F_s^* F_c]}{|\Theta(\theta)F_c|^2 + |\Theta(\theta)F_s|^2 + |(n_i/n_t)\sin\theta F_1|^2}, \tag{3}$$

where $\Theta(\theta) = \sqrt{1-(n_i^2/n_t^2)\sin^2\theta}$. F_s, F_c, and F_1 are functions of (ρ, θ), which are defined in Sec. II of the Supplemental Material [10]. In the proposed system shown

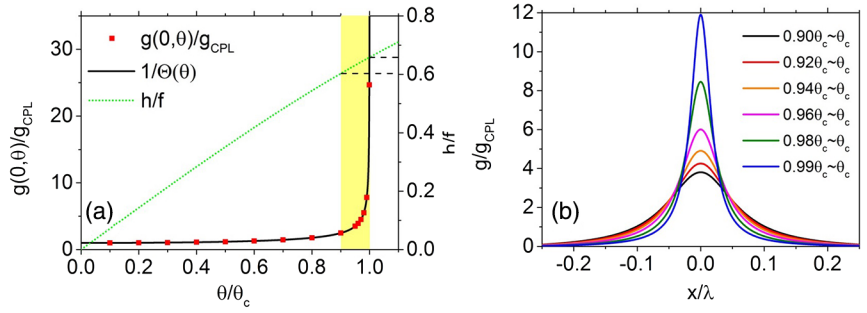

FIG. 2. (a) The g/g_{CPL} at the focus point ($\rho = 0$, $z = 0$) when the incident angle is varied from 0 to θ_c. The black curve represents the prediction function of $g(0,\theta)/g_{\mathrm{CPL}} = 1/\Theta(\theta)$, and the red dots represent the simulation results. The green dashed curve represents the sine condition of $h = f\sin\theta$. The highlighted region represents the range of incident angle $[\alpha\theta_c, \theta_c]$. (b) The lateral distribution of g/g_{CPL} for different ranges of incident angle when the topological charge of the SPP is $m = 1$.

in Fig. 1, the incident beam is focused on the glass-air interface with $n_i = 1.518$ for glass and $n_t = 1$ for air. When the incident angle θ is larger than the critical angle $\theta_c = \arcsin(n_t/n_i)$, the EM field in the air is only comprised of evanescent waves confined near the planar interface. In this case, $\Theta(\theta)$ becomes a pure imaginary value. As a result, $g(\rho,\theta)/g_{\mathrm{CPL}} = 0$, indicating that the focused field has no chirality. Therefore, the evanescent waves should be eliminated from the transmitted field by choosing the incident angle of $\theta \le \theta_c$. In this case, g/g_{CPL} of the local field at the focal point ($\rho = 0$, $z = 0$) can be simplified as $g(0,\theta)/g_{\mathrm{CPL}} = 1/\Theta(\theta)$ as shown in Fig. 2(a). One can see that when the incident angle θ approaches the critical angle θ_c, g/g_{CPL} grows dramatically. Consequently, to achieve a larger g value at the focal point, the incident angle range should be chosen as $[\alpha\theta_c, \theta_c]$, indicated by the shaded region in Fig. 2(a). The inner and outer radius of the ring aperture can be determined by cross points between the boundary of the shaded region and the green dashed curve, representing a sine condition of $h = f\sin\theta$. By controlling the α value, one can manipulate and enhance the g factor, as shown in Fig. 2(b) (all other parameters used in the calculation are provided in Sec. I in the Supplemental Material [10]). In particular, when α gets closer to 1, the dimension of the superchiral hot spot is gradually squeezed into a deep subwavelength regime with significantly enhanced chirality at the focal point. For instance, for $\alpha = 0.99$, the optical chirality is enhanced by 11.9-fold at the focal point with the full width at half maximum (FWHM) of only 0.038λ [see the blue line in Fig. 2(b)], representing the realization of a subdiffraction limit superchiral spot. When α approaches 1 further, the width of the ring aperture becomes even smaller. It should be noted that under this sine condition, the width of the ring aperture is $\Delta h \approx 54$ μm for a lens with the focal length of 1 cm. This scale is much larger than the wavelength in the visible and near-infrared regime, and is therefore practical. To further increase the optical chirality, the width of the ring aperture should be reduced. If the parameter of α is 1, the ratio of $|\mathbf{H}|/|\mathbf{E}|$ at the focus point increases dramatically, and the g factor approaches infinity theoretically according to Eq. (3). However, it should be noted that this simplified theory is only applicable when the ratio between $\mathbf{E}$-field energy density U_e and $\mathbf{H}$-field energy density U_b is much smaller than $\gamma = \mathrm{Im}(\mu_B)/c^2\mathrm{Im}(\mu_E)$. Our estimated enhancement factor of 11.9 is within this regime (similar to the one observed in experiment [5]). To accurately evaluate the g-factor enhancement, the magnetic dipole transition should be incorporated in the model as discussed by Ref. [26].

To further reveal the optical properties of the focused super chiral field, we then model the distributions of electric field, magnetic field, and g/g_{CPL} in Fig. 3 for $\alpha = 0.99$ (i.e., the integral range of $[0.99\theta_c, \theta_c]$). Figures 3(a) and 3(b) show the distribution of electric-field components ($|\boldsymbol{E}_{\parallel}|$ and $|\boldsymbol{E}_z|$) on the glass-air interface. When the incident angle of the p-polarized light is slightly smaller than θ_c, its refractive angle through the glass-air interface is $\sim 90°$. In this case, $\boldsymbol{E}_z$ is the dominant component of the electric field, and the $\boldsymbol{E}_{\parallel}$ component parallel to the interface is largely reduced [Fig. 3(a)]. As illustrated in Fig. 1(a), the $\boldsymbol{E}_z$ component at the focal point is largely suppressed due to the destructive interference. As a result, a doughnut shape $\mathbf{E}$-field spot can be obtained at the focal point [Fig. 3(b)]. On the other hand, since the $\boldsymbol{H}_z$ component does not exist in the p-polarized light, the focused spot only contains $\boldsymbol{H}_{\parallel}$-component, as shown in Fig. 3(c). Based on these types of electric- and magnetic-field distributions, g/g_{CPL} is calculated by Eq. (2) as shown in Fig. 3(d). A peak chirality enhancement factor of 11.9 is obtained with the full width at half maximum (FWHM) of 38 nm (i.e., $\sim\lambda/25$). Because of the narrow range of the incident angle θ, the transmission field can be approximately regarded as a nondiffracting Bessel beam, as shown in Figs. 3(e)–3(g): along the z direction, the lateral profiles of all EM components are almost unchanged and the field amplitudes decay slowly. Therefore, the deep-subwavelength superchiral spot shown in Fig. 3(d) is well retained along the z direction. As shown in Fig. 3(h), the deep-subwavelength region extends up to more than 10λ along the z direction, resulting in an optical

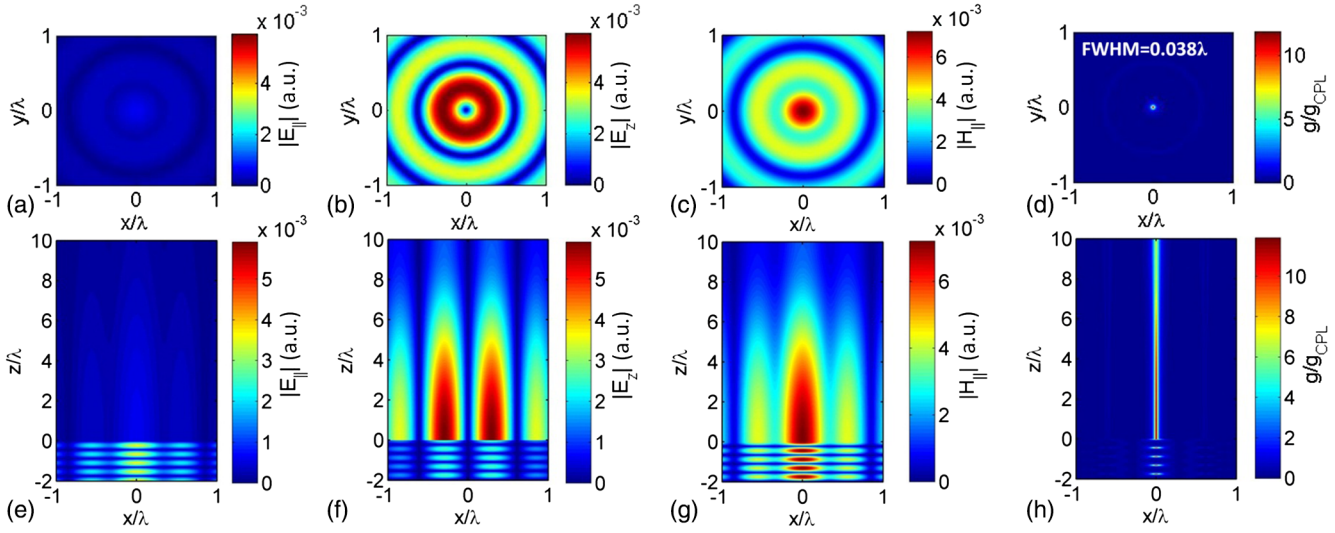

FIG. 3. (a)–(d) represent the distributions of $|\boldsymbol{E}_{\parallel}|$, $|\boldsymbol{E}_z|$, $|\boldsymbol{H}_{\parallel}|$, and g/g_{CPL} on the air-glass interface $z = 0$), respectively. (e)–(h) represent the distributions of $|\boldsymbol{E}_{\parallel}|$, $|\boldsymbol{E}_z|$, $|\boldsymbol{H}_{\parallel}|$, and g/g_{CPL} on the x-z plane ($y = 0$), respectively.

needle that is highly desired for new CD imaging applications (e.g., Refs. [27–29]). In particular, this superchiral optical needle has a great tolerance along the z axis and is promising to realize two-dimensional CD imaging of sparsely distributed single molecules.

To demonstrate the localized enhancement of g factor, we then employed the superchiral optical needle to scan three chiral molecule disks with diameters of 600, 200, and 50 nm, as shown in Figs. 4(a)–4(c), respectively. In this modeling, the chiral disk consists of large numbers of chiral molecules (as explained by Sec. III of the Supplemental Material [10]). The optical response of each chiral molecule can be described by Eq. (1). In particular, the 600-nm disk [Fig. 4(a)] and 50-nm disk [Fig. 4(c)] have left-handed

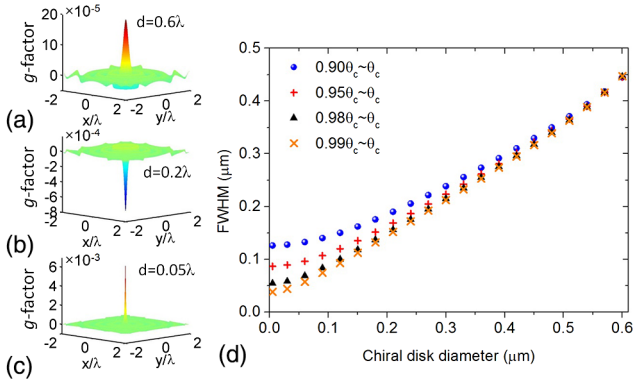

FIG. 4. The chiral imaging of nano-objects with diameters of 600, 200, and 50 nm in (a), (b), and (c), respectively. The chirality of the molecule in (b) is opposite from those in (a) and (c). The g factor of the chiral disk is calculated by $g(\mathbf{R}) = 2(A^+ - A^-)/(A^+ + A^-)$ (see Sec. III of the Supplemental Material [10]). (d) The relationship between the nano-object diameter and FWHM of the g-factor image.

chirality, while the 200-nm disk [Fig. 5(b)] has the right-handed chirality. The incident wavelength is $\lambda = 1$ μm. One can see that the size of the g-factor image obviously depends on the diameter of the disk, indicating the imaging capability of the deep-subwavelength superchiral spot needle. The CD signal of an individual chiral object is largely enhanced when its geometrical dimension approaches the diameter of the superchiral optical needle [e.g., $d = 0.05\lambda$ in Fig. 4(c)]. When the incident angles are set in the range of $[0.90\theta_c, \theta_c]$, $[0.95\theta_c, \theta_c]$, $[0.98\theta_c, \theta_c]$ and $[0.99\theta_c, \theta_c]$, respectively, their corresponding diameters of the superchiral optical needle are 126, 86, 54, and 38 nm, respectively. When these four superchiral needles are employed to scan the chiral molecule disk, the relationships between the FWHM of the g-factor image and the actual disk diameter are shown in Fig. 4(d). A smaller superchiral needle can better reveal the spatial feature of the chiral nano-object. Remarkably, the chirality of those nano-objects can also be revealed by the mapping of the g factor simultaneously. For the left-handed chiral molecule disks in Figs. 4(a) and 4(c), the g factors are positive, while for the right-handed chiral molecule disk in Fig. 4(b), the g factor is negative. Therefore, both the size and the chirality of the chiral molecule nano-objects can be mapped using this unique superchiral optical needle, which cannot be realized by any existing technology. Considering actual experimental validation, the fluorescence detected CD measurements will be more feasible [5,30]. For the two-dimensional scan, fluorescence signals from the chiral molecules should be detected under the excitation of a pair of light fields with opposite chiralities for each spatially resolved position. However, two separate spatial scans are undesirable since it requires spatial registration of two images as well as an extremely stable light source. Acquiring signals for illuminations with opposite chiralities during the same dwelling

time at a spatially revolved point is highly desirable. To be compatible with the conventional CD system, the incident RP beam through the SPP in Fig. 1(a) can be replaced by the CPL beam through radially polarized plate (see Sec. V of Supplemental Material [10]). In this alternative method, the sign of optical chirality at the focal point can be switched by changing the spin of the incident CPL beam.

The origin of the strongly localized CD enhancement is attributed by the combination of pure ED transition and mixed ED-MD transition of the nano-object [6]. For a chiral molecule whose optical response is described in Eqs. (1), its optical absorption is contributed by these two transitions expressed by Eqs. (4).

$$\Gamma_{\mathrm{ED}} = \frac{\omega}{2}\mathrm{Im}(\mu_E)|\mathbf{E}|^2 \approx \frac{\omega}{2}\mathrm{Im}(\mu_E)|\mathbf{E}_z|^2, \tag{4a}$$

$$\Gamma_{\mathrm{ED-MD}} = \omega \mathrm{Im}(G)\mathrm{Im}(\mathbf{E}\cdot\mathbf{H}^*) = \omega \mathrm{Im}(G)\mathbf{E}_{\parallel}\cdot\mathbf{H}_{\parallel}^*. \tag{4b}$$

Here, ω is the frequency of light. For the superchiral field, the $\boldsymbol{E}_z$ component is the major component of electric field (i.e., $|\mathbf{E}|^2 \approx |\boldsymbol{E}_z|^2$). Considering that the $\boldsymbol{H}_z$ component is null in the focus field, $\Gamma_{\mathrm{ED-MD}}$ [i.e., Eq. (4b)] is only determined by those field components parallel to the dielectric interface. By applying parity inversion on the incident field, in has been proven that Γ_{ED} remains unchanged while $\Gamma_{\mathrm{ED-MD}}$ becomes $-\Gamma_{\mathrm{ED-MD}}$ [3]. Therefore, Γ_{ED} is the achiral term, and $\Gamma_{\mathrm{ED-MD}}$ is the chiral term. At the focal point as shown in Fig. 3(b), the distribution of $\boldsymbol{E}_z$ component is in doughnut shape. At the center of the focal point, $\boldsymbol{E}_z = 0$ as it is the phase singular point. The chirality is largely enhanced due to the reduced achiral term of Γ_{ED}. While in the areas around the center of the focus, $\boldsymbol{E}_z$ increases significantly, resulting in the vanished chirality enhancement. In this case, the superchiral region is squeezed into a deep subwavelength scale. During the CD imaging, the chiral signal is relatively weak compared with the achiral signal, which is an intrinsic challenge of all CD measurements. Extra theoretical calculations show that the value of the g factor decreases fast when the diameter of the chiral disk increases (see Sec. VI of Supplemental Material [10]), because the strong E_z-field intensity around the focus introduces the achiral absorption term through the ED transition. Therefore, the g factor can be enhanced significantly for small chiral objects by the superchiral needle. In particular, the fluorescence detected CD measurements of single molecules [30] can be improved by the proposed method. The stimulated emission depletion technique [31] is one potential approach to reduce the achiral signal around the focus. In addition, confocal microscopy can also be employed to relieve this challenge. A confocal pinhole can be introduced in front of the detector to eliminate the ED transition signal from the donut-shaped E_z field surrounding the focus. These potential technical barriers will need to be addressed in future experimental investigation.

In conclusion, we proposed an optical system to generate a superchiral optical needle by sharply focusing twisted RP beams on a dielectric interface. By controlling the range of the incident angle, the diameter of the superchiral region can be tuned down to $\sim\lambda/25$, and the optical chirality is enhanced by 11.9-fold than that of a CPL. Moreover, the needle-shaped superchiral field was employed to map the size and the chirality of chiral molecule nanodisks simultaneously. This CD imaging capability for sparse subdiffraction objects results from the highly localized response of a chiral molecule near the focus, where the mixed ED-MD transition is enhanced, while the pure ED transition is reduced. This method has a great potential to enrich the tools of CD spectroscopy measurement and superresolution imaging by combining with other techniques (e.g., introducing plasmonic nanostructures [32–37] at the focus).

*Corresponding author.
qqgan@buffalo.edu
†Corresponding author.
qzhan1@udayton.edu

[1] L. D. Barron, *Molecular Light Scattering and Optical Activity* (Cambridge University Press, Cambridge, England, 2004).
[2] Y. Inoue and V. Ramamurthy, *Chiral Photochemistry* (Marcel Dekker, New York, 2004).
[3] Y. Tang and A. E. Cohen, Optical Chirality and Its Interaction with Matter, Phys. Rev. Lett. **104**, 163901 (2010).
[4] K. C. van Kruining, R. P. Cameron, and J. B. Götte, Superpositions of up to six plane waves without electric-field interference, Optica **5**, 1091 (2018).
[5] Y. Tang and A. E. Cohen, Enhanced enantioselectivity in excitation of chiral molecules by superchiral light, Science **332**, 333 (2011).
[6] N. Yang and A. E. Cohen, Local geometry of electromagnetic fields and its role in molecular multipole transitions, J. Phys. Chem. B **115**, 5304 (2011).
[7] C. Rosales-Guzmán, K. Volke-Sepulveda, and J. P. Torres, Light with enhanced optical chirality, Opt. Lett. **37**, 3486 (2012).
[8] R. P. Cameron and S. M. Barnett, Optical activity in the scattering of structured light, Phys. Chem. Chem. Phys. **16**, 25819 (2014).
[9] A. Canaguier-Durand and C. Genet, Chiral near fields generated from plasmonic optical lattices, Phys. Rev. A **90**, 023842 (2014).
[10] See Supplemental Material at http://link.aps.org/supplemental/10.1103/PhysRevLett.122.223901 for the details about the modeling, the numerical method employed in this work, the alternative design compatible with the conventional CD system, and further analysis of g-factor enhancement for chiral disks. The Supplemental Material includes Refs. [11–15].
[11] R. H. Jordan and D. G. Hall, Free-space Azimuthal paraxial wave equation: The Azimuthal bessel-gauss beam solution, Opt. Lett. **19**, 427 (1994).

[12] M. Gu, *Advanced Optical Imaging Theory* (Springer, Berlin, 2000).
[13] B. Richards and E. Wolf, Electromagnetic diffraction in optical systems ii. structure of the image field in an aplanatic system, Proc. Roy. Soc. A **253**, 358 (1959).
[14] M. Born and E. Wolf, *Principles of Optics*, 7th ed. (Cambridge University Press, Cambridge, England, 1999).
[15] Q. Zhan, Properties of circularly polarized vortex beams, Opt. Lett. **31**, 867 (2006).
[16] C. J. R. Sheppard and A. Choudhury, Annular pupils, radial polarization, and superresolution, Appl. Opt. **43**, 4322 (2004).
[17] G. Rui and Q. Zhan, Trapping of resonant metallic nanoparticles with engineered vectorial optical field, Nanophotonics **3**, 351 (2014).
[18] E. P. Walker and T. D. Milster, Beam shaping for optical data storage, Proc. SPIE Int. Soc. Opt. Eng. **4443**, 73 (2001).
[19] Y. I. Salamin, Mono-energetic GeV electrons from ionization in a radially polarized laser beam, Opt. Lett. **32**, 90 (2007).
[20] Q. Zhan, Cylindrical vector beams: From Mathematical concepts to applications, Adv. Opt. Photonics **1**, 1 (2009).
[21] M. Kasperczyk, S. Person, D. Ananias, L. D. Carlos, and L. Novotny, Excitation of Magnetic Dipole Transitions at Optical Frequencies, Phys. Rev. Lett. **114**, 163903 (2015).
[22] V. V. Klimov, D. Bloch, M. Ducloy, and J. R. Rios Leite, Detecting photons in the dark region of laguerre-gauss beams, Opt. Express **17**, 9718 (2009).
[23] V. V. Klimov, D. Bloch, M. Ducloy, and J. R. Rios Leite, Mapping of focused laguerre-gauss beams: The interplay between spin and orbital angular momentum and its dependence on detector characteristics, Phys. Rev. A **85**, 053834 (2012).
[24] K. Youngworth and T. Brown, Focusing of high numerical aperture cylindrical-vector beams, Opt. Express **7**, 77 (2000).
[25] J. Kim, Y. Wang, and X. Zhang, Calculation of vectorial diffraction in optical systems, J. Opt. Soc. Am. A **35**, 526 (2018).
[26] J. S. Choi and M. Cho, Limitations of a superchiral field, Phys. Rev. A **86**, 063834 (2012).
[27] L. Gao, L. Shao, B. C. Chen, and E. Betzig, 3D live fluorescence imaging of cellular dynamics using bessel beam plane illumination microscopy, Nat. Protoc. **9**, 1083 (2014).
[28] C. Snoeyink, Imaging performance of bessel beam microscopy, Opt. Lett. **38**, 2550 (2013).
[29] T. A. Planchon, L. Gao, D. E. Mikie, M. W. Davidson, J. A. Galbraith, C. G. Galbraith, and E. Betzig, Rapid three-dimensional isotropic imaging of living cells using bessel beam plane illumination, Nat. Methods **8**, 417 (2011).
[30] Y. Tang, T. A. Cook, and A. E. Cohen, Limits on fluorescence detected circular dichroism of single helicene molecules, J. Phys. Chem. A **113**, 6213 (2009).
[31] T. A. Klar, S. Jakobs, M. Dyba, A. Egner, and S. W. Hell, Fluorescence microscopy with diffraction resolution barrier broken by stimulated emission, Proc. Natl. Acad. Sci. U.S.A. **97**, 8206 (2000).
[32] M. Hentschel, M. Schäferling, X. Duan, H. Giessen, and N. Liu, Chiral plasmonics, Sci. Adv. **3**, e1602735 (2017).
[33] Y. Cui, L. Kang, S. Lan, S. Rodrigues, and W. Cai, Giant chiral optical response from a twisted-arc metamaterial, Nano Lett. **14**, 1021 (2014).
[34] Y. Zhao, A. N. Askarpour, L. Sun, J. Shi, X. Li, and A. Alu, Chirality detection of enantiomers using twisted optical metamaterials, Nat. Commun. **8**, 14180 (2017).
[35] A. Vazquez-Guardado and D. Chanda, Superchiral Light Generation on Degenerate Achiral Surfaces, Phys. Rev. Lett. **120**, 137601 (2018).
[36] K. Yao and Y. Liu, Enhancing circular dichroism by chiral hotspots in silicon nanocube dimers, Nanoscale **10**, 8779 (2018).
[37] L. V. Poulikakos, P. Thureja, A. Stollmann, E. D. Leo, and D. J. Norris, Chiral light design and detection inspired by optical antenna theory, Nano Lett. **18**, 4633 (2018).